J. Fluid Mech. (2013), *vol.* 722, *pp.* 267–290.
doi:10.1017/jfm.2013.92

Turbulent drag reduction through rotating discs

Pierre Ricco[1],† **and Stanislav Hahn**[2]

[1]Department of Mechanical Engineering, The University of Sheffield, Mappin Street, Sheffield S1 3JD, UK

[2]Honeywell Turbo Technologies, Turanka 100/1236, Brno, Czech Republic

(Received 7 October 2012; revised 24 December 2012; accepted 10 February 2013; first published online 28 March 2013)

An active technique for friction drag reduction in a turbulent channel flow is studied by direct numerical simulations. The flow modification is induced by the steady rotation of rigid flush-mounted discs, located next to one another on the walls. The effect of the disc motion on the turbulent drag is investigated at a Reynolds number of $R_\tau = 180$, based on the friction velocity of the stationary-wall case and the half channel height. For a fixed maximum disc tip velocity, drag reduction can be achieved when the disc diameter is larger than a threshold, while below this threshold the drag increases. A maximum drag reduction of 23% is computed. The net power saved, obtained by taking into account the power spent to enforce the rotational motion against the fluid viscous resistance, is found to be positive and reach 10%. The disc-flow parameters required for commercial aircraft flight conditions and flows over high-speed trains and ship hulls are estimated and future implementations based on existing micro-electromagnetic motor and micro-air turbine technologies are discussed.

Key words: drag reduction, flow control, turbulent boundary layers

1. Introduction

Turbulent drag reduction represents one of the great challenges in modern fluid mechanics research and an opportunity to facilitate the immense energy savings that could be achieved in numerous industrial applications. The need for lower fuel consumption and improved environmental sustainability has driven large efforts in the academic and industrial worlds to study new drag-reduction techniques.

Amongst the open-loop active methods (for which energy is input to the system to modify the flow in a predetermined manner), the technique of spanwise wall oscillations has experienced a growing interest since first studied by Jung, Mangiavacchi & Akhavan (1992). They showed that drag reduction can be achieved if the wall below a turbulent flow oscillates in time along the spanwise direction according to $w = W\sin(2\pi t/T)$, where T is the oscillation period. The low-speed streaks, recognized as key players in the near-wall turbulence dynamics, are cyclically tilted to an angle and dragged laterally by the wall. This results in a suppressed sweeping and bursting activity, which is instrumental in the reduction of turbulent kinetic energy (Ricco 2004). An optimal period of oscillation, $T^+_{opt} \approx 120$ (where $+$ here indicates scaling by viscous units of the stationary-wall case), has been found for

† Email address for correspondence: p.ricco@sheffield.ac.uk

a fixed W and a drag reduction as large as 45% is obtained when W is comparable with the free-stream velocity of a turbulent boundary layer (Choi, DeBisschop & Clayton 1998). Research has also been carried out to model the near-wall flow and to explain the drag-reduction mechanism (Dhanak & Si 1999; Choi 2002; Duque-Daza *et al.* 2012; Moarref & Jovanovic 2012).

Inspired by the oscillating-wall technique, Viotti, Quadrio & Luchini (2009) have converted the unsteady motion into a steady streamwise-dependent forcing, i.e. $w = W\sin(2\pi x/\lambda)$, where λ is the wavelength of forcing. Their direct numerical simulations have shown that, analogously to the unsteady case, an optimal wavelength for drag reduction exists, $\lambda^+_{opt} \approx 1250$, which is related to T^+_{opt} through $\lambda_{opt} = \mathscr{U}_w T_{opt}$, where $\mathscr{U}_w$ is the near-wall turbulent convection velocity. A maximum of 50% drag reduction was found for $W^+ = 20$ and the maximum net power saved was 23% (computed by subtracting the power employed to move the wall against the viscous flow resistance from the power saved thanks to the wall motion).

Although these methods are interesting for their large drag reduction, the net power saved, and as test cases for studying the drag-reduction mechanism (Choi & Clayton 2001; Ricco *et al.* 2012), their practical realization clearly remains a major challenge. Important steps in this direction are the experimental works by Auteri *et al.* (2010), where drag reduction was achieved through the unsteady rotation of pipe sections, and by Gouder, Potter & Morrison (2013), who forced the wall turbulence by in-plane, high-frequency oscillatory deflections of an electroactive polymer. The implementation of spanwise-moving wall sections in systems of technological importance, such as flows over aircraft wings and turbine blades, however, appears elusive in the foreseeable future. One of the main reasons for this lies in the estimated oscillation frequency corresponding to $T^+_{opt} = 120$ being extremely high, i.e. about 15 kHz over the wing of a commercial aircraft at a cruise speed of 225 m s^{-1} at 10 km above sea level (the friction velocity $u_\tau = 8$ m s^{-1} and the kinematic viscosity $\nu = 35 \times 10^{-6}$ m^2 s^{-1}).

A related novel device proposed by Keefe (1997, 1998), based on wall-normal vorticity forcing, may instead offer exciting opportunities for industrial applications. This actuator consists of arrays of discs which are flush-mounted on a flat surface and rotate at constant angular velocity. To the best of our knowledge, neither experimental nor numerical studies exist on this type of flow. Our objective is to investigate the effects of the disc diameter and rotational frequency on the near-wall turbulence by means of direct numerical simulations in the channel flow geometry. The focus is on the turbulent friction drag and on the net power saved.

The numerical procedures are presented in § 2. The computational solver, scaling procedures, disc arrangement, discretization parameters and averaging procedures are contained in §§ 2.1–2.4. Section 2.5 outlines the numerical resolution checks. The results are presented in § 3. The dependence of drag reduction on the wall forcing parameters is discussed in § 3.1. In §§ 3.2 and 3.3, the disc flow is visualized and the turbulence statistics are studied. The role of the period of rotation and the disc-flow viscous layer thickness is discussed in § 3.4, while results on the power spent to drive the disc motion and on the net power saved are given in § 3.5. A discussion on the applicability of the disc-flow technique to flows of technological interest is found in § 4.

2. Numerical procedures

2.1. *Numerical solver of the Navier–Stokes equations*

A pressure-driven turbulent flow between infinite parallel flat plates at a low Reynolds number has been studied by direct numerical simulations. The open-source numerical code available on the Internet (Gibson 2006) has been modified to impose the rotation of the discs on the walls. The code solves the incompressible Navier–Stokes equations in the channel flow geometry using Fourier series expansions along the streamwise (x) and spanwise (z) homogeneous directions, and Chebyshev polynomials along the wall-normal direction (y). The numerical method is based on the Kleiser–Schumann algorithm (Kleiser & Schumann 1980), also used in Gibson, Halcrow & Cvitanovic (2008) and described in Canuto *et al.* (1988). The time-stepping algorithm, reported in Ascher, Ruuth & Wetton (1995), is based on a third-order semi-implicit backward differentiation scheme (SBDF3), which treats the nonlinear terms explicitly and the linear terms implicitly. According to Gibson (2006), SBDF3 is set as default in the code as it is the most efficient amongst the third-order implicit–explicit multi-step schemes available for the code. Dealiasing is performed at each time step by setting to zero the upper one-third of the Fourier coefficients along the streamwise and spanwise directions. The calculations have been run in parallel using an OpenMP strategy on the computer cluster Iceberg at the University of Sheffield.

2.2. *Scaling of flow quantities*

Dimensional quantities are henceforth indicated by the symbol $*$. Lengths are scaled by h^*, the half channel height, velocities are scaled by U_p^*, the maximum centreline velocity of the laminar Poiseuille flow at the same mass flow rate, time is made dimensionless by h^*/U_p^*, and pressure by $\rho^* U_p^{*2}$, where ρ^* is the density. Quantities scaled by these outer units are not marked by any symbol. The symbol $+$ denotes scaling by the viscous inner units of the flow, i.e. by the kinematic viscosity ν^* and the friction velocity $u_\tau^* = \sqrt{\tau_w^*/\rho^*}$, where τ_w^* is the space- and time-averaged wall-shear stress.

2.3. *Arrangement of discs*

The flow domain is shown in figure 1. The discs are located next to one another, have a diameter D and rotate at a constant angular velocity Ω with tip velocity $W = \Omega D/2$. Discs which are next to each other along x have opposite direction of rotation, while the direction of rotation along rows in the z direction is the same. Due to the domain periodicity and the alternate sense of rotation along x, an even number of discs is enforced in this direction. A triangular wave of spanwise velocity is generated along lines parallel to x and connecting the disc centres. This disc configuration has been chosen to mimic the standing-wave forcing by Viotti *et al.* (2009). The two drag-reduction techniques however differ considerably because in Viotti *et al.* (2009)'s case the wall forcing is sinusoidal, uniform along z, only oriented along the spanwise direction, and covers the entire wall surface. The wall velocity is first assigned in the physical space and then transformed into the spectral space to create the Fourier mode representation. Dirichlet boundary conditions are imposed on the equations of motion of the modes.

A thin buffer annular region around each disc is simulated, as shown in figure 1. The percentage ratio between the clearance c and the disc radius if the clearance were not present, $100 \times 2c/(2c + D)$, is 6% for $D = 0.84$, 1.67, 5% for $D = 3.38$, 5.07, 4% for $D = 6.83$ and 3% for $D = 8.62$, 10.35. A larger annular region is used for smaller

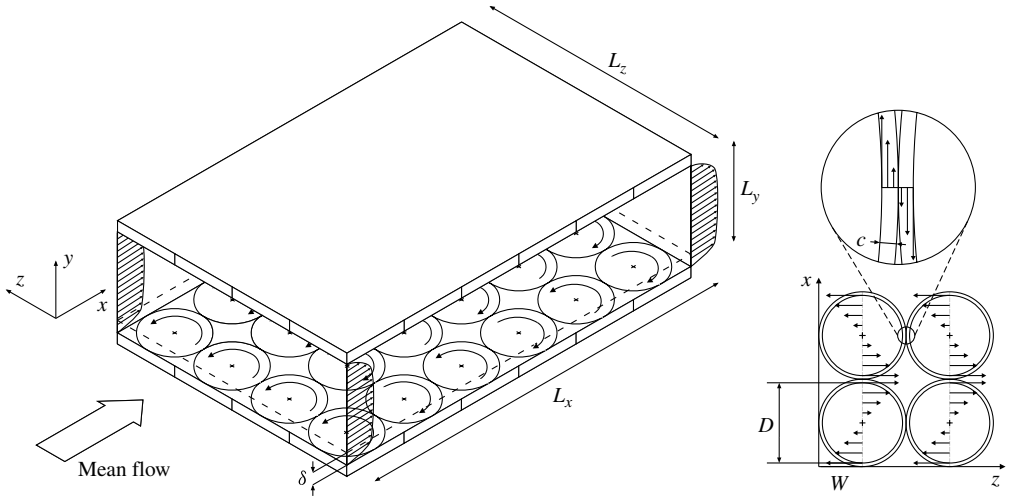

FIGURE 1. Schematic of the turbulent channel flow with rotating discs. The z-component of the wall velocity along lines parallel to x and passing through the disc centres.

diameters in order to avoid spurious oscillations at the boundary between the discs and stationary wall as discussed below. The velocity field in this region is assumed to be independent of the azimuthal angle and to decrease linearly from the maximum at the disc tip to zero at the stationary wall, i.e. the wall tangential velocity w_r varies with the radial coordinate r, measured from the centre of each disc, as follows:

$$w_r(r) = \begin{cases} 2Wr/D, & r \leqslant D/2 \\ W(c - r + D/2)/c, & D/2 \leqslant r \leqslant D/2 + c. \end{cases} \tag{2.1}$$

The simulation of this region is useful for two reasons. It provides an idealized representation of the gap between the spinning disc and the stationary wall, which would be inevitably present in a laboratory apparatus. The other crucial advantage brought about by simulating the clearance is that, as the wall velocity at $y = 0$ and $y = 2$ is now continuous, the Gibbs phenomenon is strongly reduced, provided that a sufficient number of Fourier modes is utilized. The spurious oscillations would always occur if the clearance were not simulated because of the velocity discontinuity between the disc tip and the stationary wall. Figure 2(a) shows that, for $D = 0.84$, $W = 0.77$, no Gibbs-type oscillations occur in the wall streamwise velocity, shown as a function of z at $x = D/2$. This is the location with the highest velocity jump between neighbouring discs for the case with the largest number of discs in the computational domain, and therefore this is the case which is most prone to spurious oscillations. Figure 2(b) shows the same quantity for $D = 5.07$, $W = 0.39$, which yields the highest drag reduction of 22.9%.

The strategy of simulating a region where the wall velocity changes linearly has already been employed successfully by other researchers. Kannepalli & Piomelli (2000) used a quite long adjustment region to study spanwise-shear-driven wall turbulence. Skote (2012) recently simulated a turbulent boundary layer altered by a finite-length spanwise-oscillating wall; a thin region was simulated between the stationary wall and the moving wall, where the velocity increased linearly. Skote (2012)'s approach is in line with ours as the adjustment region was intended to

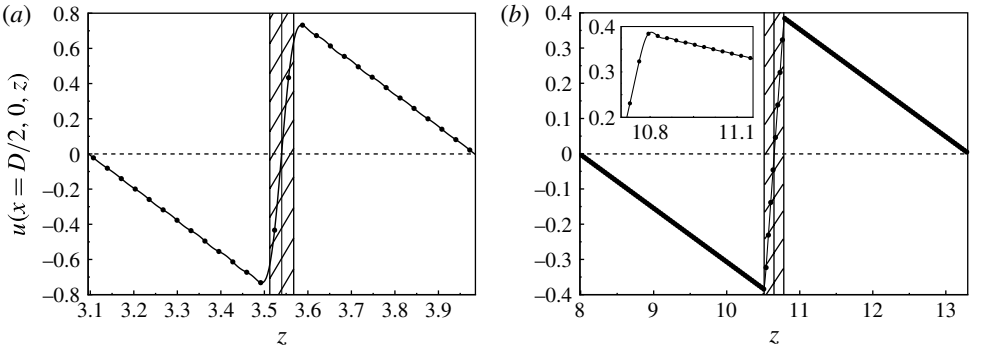

FIGURE 2. Profile of streamwise wall velocity versus z at $x = D/2$. (*a*) $D = 0.84$, $W = 0.77$ ($D^+ = 188$, $W^+ = 14.4$). (*b*) $D = 5.07$, $W = 0.39$ ($D^+ = 801$, $W^+ = 10.2$). Circles indicate data at grid points, while solid lines show the continuous representation of velocity by Fourier series. The oblique lines denote the clearance.

suppress the Gibbs phenomenon. One could implement more realistic boundary conditions by modelling the flow through the clearance and/or by simulating the turbulent channel flow and the clearance flow as coupled systems, although these objectives lie outside the scope of the present study.

2.4. *Numerical parameters and averaging procedures*

The simulations have been performed at a constant mass flow rate and at a Reynolds number $R_p = U_p^* h^*/\nu^* = 4200$. The stationary-wall friction Reynolds number is $R_{\tau,s} = u_\tau^* h^*/\nu^* = 179.8$ (where the subscript s indicates stationary-wall conditions). The dimensions of the computational domain are $L_x = 6.79\pi$, $L_y = 2$, and $L_z = 2.26\pi$, i.e. $L_x^+ = 3840$, $L_y^+ = 360$, and $L_z^+ = 1280$ (viscous inner units of the stationary-wall case are used henceforth in this section, unless otherwise stated). The numbers of Fourier modes are $N_x = 334$ along x and $N_z = 222$ along z, providing spatial resolutions of $\Delta x^+ = 11.5$ and $\Delta z^+ = 5.75$. Because of the truncation of the upper one-third of the Fourier modes to avoid dealiasing, the spatial resolution is not purely spectral. The Nyquist critical wavelengths are thus $\lambda_{Nx}^+ = 3\Delta x^+$ and $\lambda_{Nz}^+ = 3\Delta z^+$, instead of $\lambda_{Nx}^+ = 2\Delta x^+$ and $\lambda_{Nz}^+ = 2\Delta z^+$ in the purely spectral case. Nevertheless, the resolution checks in § 2.5 show the robustness and accuracy of our computations. Larger box sizes have been used for $D = 5.07$ and 10.35, $L_x = 6.79\pi$, $L_z = 3.4\pi$ ($N_z = 334$, $L_z^+ = 1926$), and for $D = 6.83$, $L_x = 9.05\pi$, $L_z = 2.26\pi$ ($N_x = 446$, $L_x^+ = 5118$). The number of modes has been adjusted to keep the same resolution for all cases. Along y, $N_y = 129$ collocation points have been used along a stretched grid with resolution of $\Delta y_{min}^+ = 0.054$ near the wall and $\Delta y_{max}^+ = 4.42$ at the centreline. The time step varied between $\Delta t_{min}^+ = 0.008$ and $\Delta t_{max}^+ = 0.08$ to minimize the computational cost by maximizing the CFL number within the specified range, i.e. $0.2 < \mathrm{CFL} < 0.4$.

A total of 50 cases were run, for which W and D were varied independently in the parameter range $0.064 \leqslant W \leqslant 0.77$, $0.84 \leqslant D \leqslant 10.35$. The computations were initiated from a fully developed turbulent flow with stationary walls. The flow experienced a transient state of up to about $250h^*/U_p^*$ ($1950\nu^*/u_\tau^{*2}$) before reaching its new fully developed regime. Turbulence statistics were computed by averaging instantaneous flow fields at intervals of $30\nu^*/u_\tau^{*2}$ for a minimum total time of $1150h^*/U_p^*$ ($8870\nu^*/u_\tau^{*2}$) and a maximum total time of $1350h^*/U_p^*$ ($10\,400\nu^*/u_\tau^{*2}$)

L_x	L_z	Δx^+	Δz^+	N_y	$t_f - t_i$	$R_{\tau,s}$	$C_{f,s} \times 10^3$	$\lvert\Delta C_{f,s}\rvert$ (%)
6.79π	2.26π	11.5	5.75	129	1450	179.8	8.25	—
6.79π	2.26π	11.5	5.75	129	*725*	179.8	8.24	0.07
5.65π	*2.82π*	12	6	129	1450	180.1	8.28	0.35

TABLE 1. Absolute values of $\Delta C_{f,s}$, the percentage changes of $C_{f,s}$ with respect to the top case in the table, for the stationary-wall case and different discretization parameters. In this table and in the following ones, the parameters which are different from the reference cases in § 2.4, the top cases in the tables, are highlighted in italics.

after the transient has elapsed. All statistical samples were doubled by averaging over the two channel halves, and therefore the wall-normal coordinate for the averaged quantities extends from the wall at $y = 0$ to the channel centreline at $y = 1$. By defining

$$\langle \boldsymbol{f} \rangle \equiv \frac{1}{L_x L_z} \int_0^{L_z} \int_0^{L_x} \boldsymbol{f} \, \mathrm{d}x \, \mathrm{d}z, \quad \overline{\boldsymbol{f}} \equiv \frac{1}{t_f - t_i} \int_{t_i}^{t_f} \boldsymbol{f} \, \mathrm{d}t, \tag{2.2}$$

where t_i and t_f denote the start and finish averaging time, the flow field is expressed as $\boldsymbol{u}(x, y, z, t) = \boldsymbol{u}_m + \boldsymbol{u}_d + \boldsymbol{u}_t$, where $\boldsymbol{u}_m(y) = \{u_m, 0, 0\} = \langle \overline{\boldsymbol{u}} \rangle$ is the mean flow, $\boldsymbol{u}_d(x, y, z) = \{u_d, v_d, w_d\} = \overline{\boldsymbol{u}} - \boldsymbol{u}_m$ is the disc flow, and $\boldsymbol{u}_t(x, y, z, t)$ represents the turbulent fluctuations. The drag reduction is defined as $\mathscr{R}\,(\%) \equiv 100[1 - u'_m(0)/u'_{m,s}(0)]$, where the prime indicates differentiation with respect to y. The bulk velocity is defined as

$$U_b \equiv \int_0^1 u_m(y) \, \mathrm{d}y. \tag{2.3}$$

As the flow is studied at constant mass flow rate, $U_b = 2/3$.

2.5. *Resolution checks*

The $R_{\tau,s} = 179.8$ value computed here is 1% different from the value found by the correlation $R_{\tau,s} = 0.11593 R_p^{0.88} = 178.9$, given on page 279 in Pope (2000), and 0.6% different from the value found by the correlation $R_{\tau,s} = 0.12219 R_p^{0.875} = 180.9$, given on page 117 in Lesieur (1997). The skin-friction coefficient for the stationary-wall case, $C_{f,s} = 2/U_b^{+2} = 8.25 \times 10^{-3}$ differs by 1% from the value computed by Kim, Moin & Moser (1987) and by 1.3% from the value found by the empirical correlation $C_{f,s} = 0.0336 R_{\tau,s}^{-0.273}$ (Pope 2000). Table 1 shows that the percentage difference between the $C_{f,s}$ value in the reference case (top case in table 1) and cases where the discretization parameters have been changed is smaller than 1%.

The resolution checks on a case which gives a large drag reduction and on the case which leads to the highest drag increase are presented in tables 2 and 3, respectively. The percentage changes of C_f with respect to the reference case (top case in table 2) for the large drag-reduction case are small and a conservative estimate of the $\mathscr{R}$ value is $\mathscr{R} = 19.5 \pm 0.3\%$. The percentage changes in C_f for the drag-increase case is higher than for the drag-reduction case, although still smaller than 1%. This is expected because the number of discs within the computational domain is larger and therefore the resolution smaller. A conservative estimate is $\mathscr{R} = -55.8 \pm 1\%$. It is evident from the results presented in tables 2 and 3 that the wall-shear stress numerical values are robust and reliable.

Phase	L_x	L_z	Δx^+	Δz^+	N_y	$t_f - t_i$	$C_f \times 10^3$	$\lvert\Delta C_f\rvert$ (%)	$\mathscr{R}$ (%)
In	6.79π	2.26π	11.5	5.75	129	1350	6.64	—	19.5
In	6.79π	2.26π	11.5	5.75	129	*675*	6.65	0.09	19.4
In	*4.52*π	2.26π	11.5	5.75	129	1350	6.63	0.18	19.6
In	6.79π	2.26π	*8*	5.75	129	1350	6.65	0.09	19.4
In	6.79π	2.26π	11.5	*4*	129	1350	6.63	0.18	19.6
In	6.79π	2.26π	11.5	5.75	*161*	1350	6.65	0.13	19.4
In	*4.52*π	*3.34*π	11.5	5.75	129	1350	6.64	0.11	19.6
In	6.79π	*1.13*π	11.5	5.75	*257*	1350	6.64	0.11	19.6
Out	6.79π	2.26π	11.5	5.75	129	1350	6.65	0.16	19.3

TABLE 2. Absolute values of ΔC_f, the percentage changes of C_f with respect to the top case in the table, for $W = 0.39$, $D = 3.38$ and different discretization parameters (viscous units of the stationary-wall case are used here and in table 3). In this table and in table 3, the first column on the left indicates whether discs at the same (x, z) location and on opposite walls spin in phase or out of phase.

Phase	L_x	L_z	Δx^+	Δz^+	N_y	$t_f - t_i$	$C_f \times 10^3$	$\lvert\Delta C_f\rvert$ (%)	$\mathscr{R}$ (%)
In	6.79π	2.26π	11.5	5.75	129	1350	12.85	—	−55.8
In	6.79π	2.26π	11.5	5.75	129	*675*	12.86	0.05	−55.9
In	*4.52*π	2.26π	11.5	5.75	129	1350	12.82	0.27	−55.4
In	6.79π	2.26π	*8*	5.75	129	1350	12.93	0.55	−56.7
In	6.79π	2.26π	11.5	*4*	129	1350	12.79	0.52	−55
In	6.79π	2.26π	11.5	5.75	*161*	1350	12.85	0.01	−55.8
In	6.79π	*1.13*π	11.5	5.75	*257*	1350	12.88	0.23	−56.2
Out	6.79π	2.26π	11.5	5.75	129	1350	12.83	0.15	−55.6

TABLE 3. Absolute values of ΔC_f, the percentage changes of C_f with respect to the top case in the table, for $W = 0.77$ and $D = 0.84$ and different discretization parameters.

Forcing		W	D	$\mathscr{R}$ (%)
Two walls	Two-wall average	0.39	3.38	19.5
One wall	Forced wall	0.39	3.38	18.7
	Unforced wall	0.39	3.38	1.7
Two walls	Two-wall average	0.77	1.67	−33.7
One wall	Forced wall	0.77	1.67	−32.7
	Unforced wall	0.77	1.67	0.6

TABLE 4. Drag-reduction and drag-increase values obtained by imposing the disc motion on two walls and on one wall only.

The last line in tables 2 and 3 denotes cases for which discs at the same (x, z) location and on opposite walls have opposite sense of rotation. The changes of C_f with respect to the in-phase cases are within the uncertainty range obtained by changing the discretization parameters, so the effect of the sense of rotation cannot be inferred. Table 4 reports the $\mathscr{R}$ values when discs spin on one wall only. Both the drag-reduction and drag-increase values decrease by about 1%. Drag reduction was measured on the stationary walls, although in the second case the value was within the estimated uncertainty range.

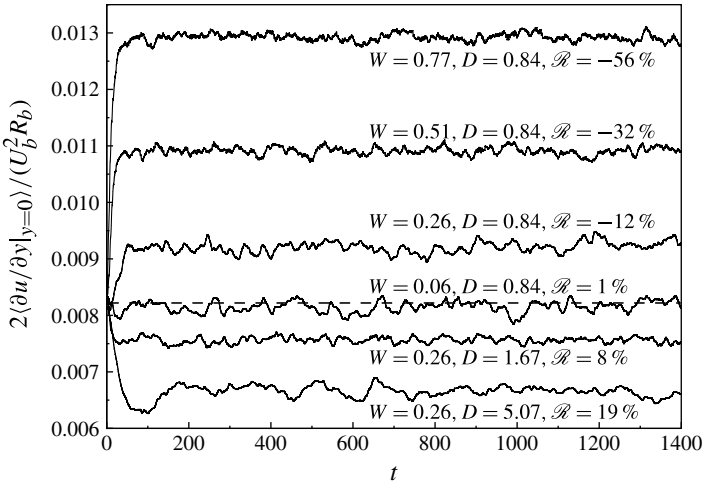

FIGURE 3. Temporal evolution of space-averaged streamwise wall friction for drag-reduction and drag-increase cases. The dashed line indicates the value of the stationary-wall skin-friction coefficient.

The code was further tested by applying spatially uniform spanwise wall oscillations, $w^+ = W^+ \sin(2\pi t^+/T^+)$, with $R_\tau = 180$, $W^+ = 12$ and $T^+ = 100$ (scaled by stationary-wall viscous units). The measured drag reduction was $\mathscr{R} = 34.4\%$, which compares well with $\mathscr{R} = 34\%$ computed recently by Quadrio's group (Gatti 2011) and with $\mathscr{R} = 32.8\%$ obtained by Quadrio & Ricco (2004) (both simulations were run at $R_\tau = 200$).

3. Results and discussion

The main quantities obtained from the simulations are reported in table 5. The power budget quantities $\mathscr{P}_{sp,t}$, $\mathscr{P}_{net}$, and $\mathscr{G}$ are defined in § 3.5 and the disc-flow boundary layer thickness δ is defined in § 3.4. The case investigated in §§ 3.2 and 3.3 is for $D = 3.38$ and $W = 0.39$ ($D^+ = 546$ and $W^+ = 10$, $\mathscr{R} = 19.5\%$, case 24 in table 5).

The temporal evolution of space-averaged streamwise wall friction of drag-reduction and drag-increase cases from the start-up of the disc motion is depicted in figure 3. The friction changes quickly for cases showing drag increase and low drag reduction, while the adjustment to the wall forcing is slower for the large drag-reduction cases.

3.1. *Turbulent drag reduction as a function of diameter D and tip velocity W*

Figure 4 shows three-dimensional maps of $\mathscr{R}(D, W)$ (%) (*a*) and $\mathscr{R}(D^+, W^+)$ (%) (*b*), where the size of the circles is proportional to the absolute value of $\mathscr{R}$. For fixed W, drag reduction occurs when D is larger than a threshold, while the drag increases for smaller D (the hatched areas denote drag-increase cases). The threshold D for drag reduction (indicated by the dashed line bounding the hatched areas), the optimal D at fixed W and the optimal W at fixed D (denoted by black dots and open circles respectively in figure 4*b*) all increase with W. The profile of optimum D at a fixed W follows closely the zero-$\mathscr{R}$ profile and is shifted by about 600 viscous units to the right. An overall maximum $\mathscr{R} = 22.9\%$ is computed for $D = 5.07$ and $W = 0.39$ ($D^+ = 801$ and $W^+ = 10.2$), which is case 25 in table 5. The graphs in figure 5 present

Case	W	D	$\mathscr{T}$	$\mathscr{R}$ (%)	$\mathscr{P}_{sp,t}$ (%)	$\mathscr{P}_{net}$ (%)	$\mathscr{G}$	δ^+	W^+	D^+	$\mathscr{T}^+$	t_i
1	0.06	0.84	40.8	1.1	1	0.6	1.2	5.3	1.5	150	311	50
2	0.06	1.67	81.7	2.3	0.8	1.9	2.9	6.7	1.5	297	616	50
3	0.06	3.38	165.1	2.7	0.6	2.5	4.3	8.6	1.5	600	1239	50
4	0.06	5.07	247.6	2.3	0.5	1.7	4.2	10	1.5	902	1866	50
5	0.06	6.83	333.6	2.3	0.5	1.8	4.6	11.2	1.5	1215	2515	50
6	0.06	8.62	421.4	1.9	0.5	1.4	4.2	12.1	1.5	1537	3189	50
7	0.06	10.35	505.6	1.7	0.4	1.3	4.0	13.1	1.5	1847	3834	50
8	0.13	0.84	20.4	0.5	3.9	−3	0.1	5.4	3	150	157	50
9	0.13	1.67	40.8	6.4	3.1	3.7	2	6.6	3.1	291	295	50
10	0.13	3.38	82.5	8.3	2.5	6.2	3.3	8.3	3.1	582	584	50
11	0.13	5.07	123.8	7.7	2.2	5.6	3.6	9.7	3.1	876	881	50
12	0.13	6.83	166.8	6.6	2	4.6	3.4	10.9	3.1	1188	1202	50
13	0.13	8.62	210.7	5.9	1.8	4.1	3.3	12	3.1	1506	1530	50
14	0.13	10.35	252.8	5.1	1.7	3.5	3.1	13	3.1	1814	1850	150
15	0.26	0.84	10.2	−11.6	16.3	−28	−0.7	5.5	5.7	159	88	50
16	0.26	1.67	20.4	8.3	12.8	−4.1	0.6	6.4	6.3	288	144	50
17	0.26	3.38	41.3	17.6	10.1	7.8	1.7	7.8	6.6	552	262	150
18	0.26	5.07	61.9	19.2	8.6	10.5	2.2	9.1	6.7	820	386	150
19	0.26	6.83	83.4	17.1	7.8	9.3	2.2	10.3	6.6	1189	533	150
20	0.26	8.62	105.3	15.4	7.2	8.2	2.1	11.4	6.5	1427	687	150
21	0.26	10.35	126.4	13.4	6.7	6.6	2.0	2.4	6.4	1733	845	150
22	0.39	0.84	6.8	−22.7	38.9	−61.1	−0.6	5.5	8.1	167	64	100
23	0.39	1.67	13.6	1	29.9	−28.5	0	6.5	9	299	104	50
24	0.39	3.38	27.5	19.5	23.3	−3.8	0.8	7.4	10	546	171	50
25	0.39	5.07	41.3	22.9	19.8	3.1	1.2	8.7	10.2	801	245	150
26	0.39	6.83	55.6	21.8	17.9	3.9	1.2	9.8	10.2	1087	335	200
27	0.39	8.62	70.2	20.6	16.6	4	1.2	10.7	10.1	1383	430	200
28	0.39	10.35	84.3	19.0	15.5	3.5	1.2	11.7	10	1677	527	225
29	0.51	0.84	5.1	−32.3	74.7	−106.4	−0.4	5.3	10.4	173	52	50
30	0.51	1.67	10.2	−8.9	56.8	−65.2	−0.2	6.3	11.5	314	86	100
31	0.51	3.38	20.6	12.3	43.5	−30.8	0.3	7.5	12.8	570	140	150
32	0.51	5.07	31	19.2	37	−17.8	0.5	8.5	13.3	820	193	150
33	0.51	6.83	41.7	21.7	33.3	−11.5	0.7	9.4	13.6	1087	252	250
34	0.51	8.62	52.7	22.2	30.9	−8.7	0.7	10.1	13.6	1369	316	250
35	0.51	10.35	63.2	20.5	29.1	−8.6	0.7	10.8	13.5	1660	387	230
36	0.64	0.84	4.1	−43.2	128.3	−170.9	−0.3	4.9	12.5	180	45	50
37	0.64	1.67	8.2	−20.1	97.2	−117.3	−0.2	6.1	13.7	330	252	100
38	0.64	3.38	16.5	3.8	73.9	−70.1	0.1	7.2	15.3	596	123	150
39	0.64	5.07	24.8	13.6	62	−48.4	0.2	8.2	16.1	848	165	140
40	0.64	6.83	33.4	17.2	55.4	−38.2	0.3	9	16.5	1118	213	250
41	0.64	8.62	42.1	20.8	51.5	−30.7	0.4	9.5	16.9	1381	258	250
42	0.64	10.35	50.6	19.9	48.3	−28.4	0.4	10.2	16.8	1667	313	250
43	0.77	0.84	3.4	−55.8	204.7	−260.5	−0.3	4.7	14.4	188	41	50
44	0.77	1.67	6.8	−33.7	154.1	−187.8	−0.2	5	15.3	348	70	70

TABLE 5. (Continued on next page)

Case	W	D	$\mathscr{T}$	$\mathscr{R}$ (%)	$\mathscr{P}_{sp,t}$ (%)	$\mathscr{P}_{net}$ (%)	$\mathscr{G}$	δ^+	W^+	D^+	$\mathscr{T}^+$	t_i
45	0.77	3.36	13.8	−6.1	115.4	−121.5	−0.1	7	17.5	626	112	100
46	0.77	5.07	20.6	6	96.3	−90.3	0.1	7.9	18.6	884	150	120
47	0.77	6.83	27.8	12.1	86.3	−74.3	0.1	8.6	19.2	1152	189	250
48	0.77	8.62	35.1	14.1	79.6	−65.5	0.2	9.3	19.4	1439	233	250
49	0.77	10.35	42.1	12.4	75.3	−62.8	0.2	9.9	19.2	1743	284	250

TABLE 5. Disc-flow forcing conditions and power budget data. The final averaging time is $t_f = 1400$ for all cases.

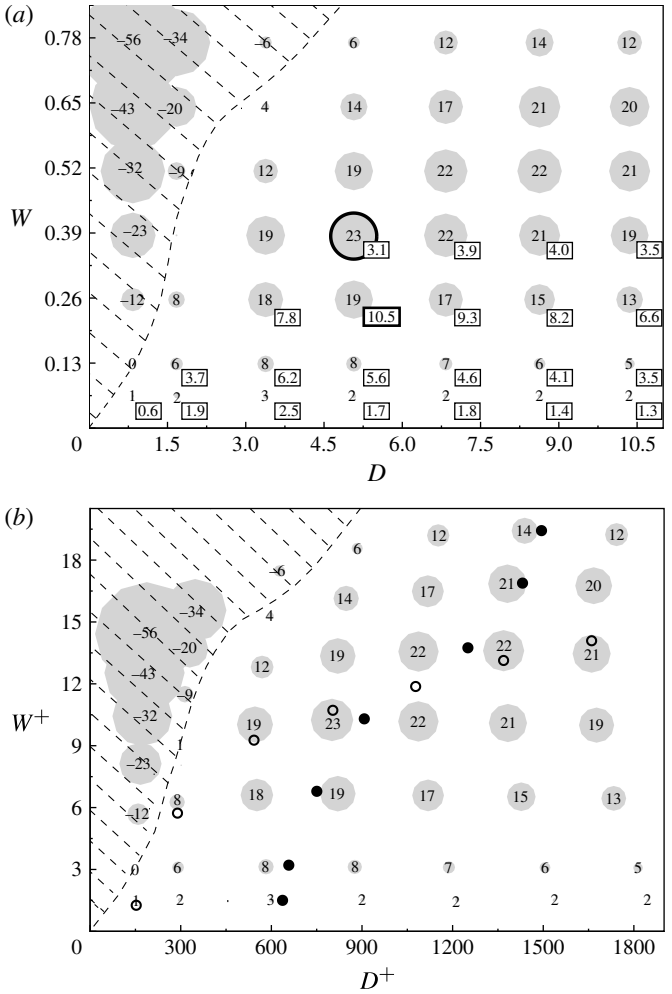

FIGURE 4. Maps of (*a*) $\mathscr{R}(D, W)$ (%) and (*b*) $\mathscr{R}(D^+, W^+)$ (%). The size of the grey circles is proportional to the absolute value of $\mathscr{R}$. The hatched areas highlight the drag-increase cases and the zero-$\mathscr{R}$ lines delimiting the hatched areas are found by linear data interpolation. In (*a*), the maximum $\mathscr{R} = 22.9\%$ is circled and the boxed values report the positive net power saved $\mathscr{P}_{net}$ (%), studied in § 3.5 (the thick box denotes the maximum $\mathscr{P}_{net} = 10.5\%$). In (*b*), the black dots indicate the estimated D for maximum $\mathscr{R}$ at fixed W and the open circles denote the estimated W for maximum $\mathscr{R}$ at fixed D.

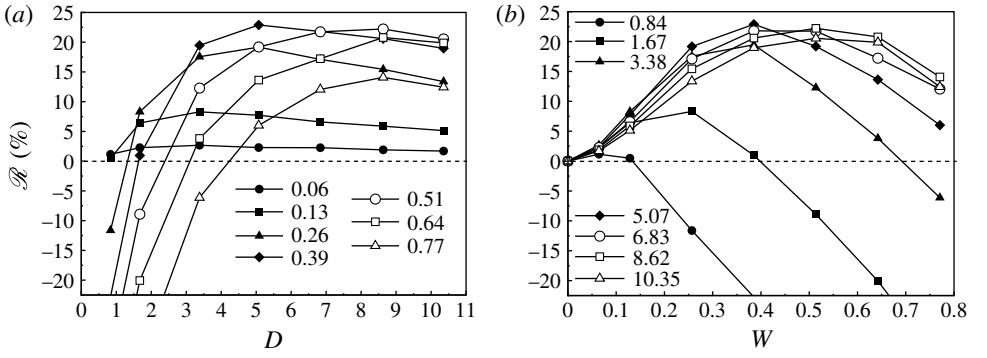

FIGURE 5. (*a*) $\mathscr{R}(D; W)$ (%); (*b*) $\mathscr{R}(W; D)$ (%). The values of W (in *a*) and D (in *b*) are given in the legends.

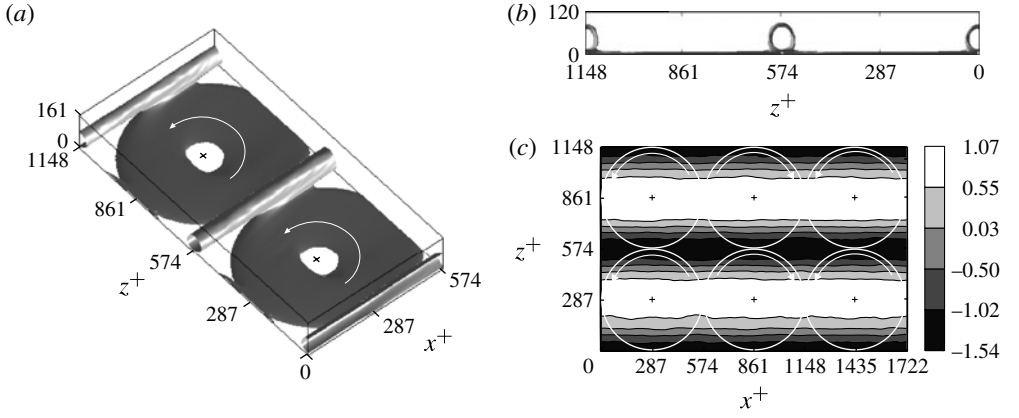

FIGURE 6. Visualizations of the time-averaged disc flow $\boldsymbol{u}_d$. (*a*) Isosurfaces of $q^+(u_d^+, w_d^+) \equiv \sqrt{u_d^{+2} + w_d^{+2}} = 2.3$, where one sixth of the domain is shown along x. (*b*) The same isosurfaces observed from the y–z plane at $x^+ = 0$. (*c*) Contour plot of u_d^+ in the centreline x–z plane; half of the domain is shown along x.

the drag change data as a function of D for a fixed W (*a*) and as a function of W for a fixed D (*b*). For a fixed D the drag reduction increases with W from zero to an optimum, then drops, and drag increase eventually occurs. For a fixed W, the drag reduction decreases slowly for diameters larger than the optimum, which agrees with the finding by Willis, Hwang & Cossu (2010) of a plateau region for drag reduction when the near-wall turbulence is forced at large spanwise scales. The occurrence of drag increase at small diameters and of high drag reduction for D^+ between about 500 and 1800 also confirms the results by Willis *et al.* (2010). They reported an increase in wall-shear stress when the spanwise-forcing length scale matched the average spanwise spacing of the low-speed streaks, $\lambda_z^+ \approx 100$, and maximum drag reduction for forcing scales between 400 and 800 viscous units.

3.2. *Flow visualization of the time-averaged disc flow*

Three-dimensional isosurfaces of $q^+(u_d^+, w_d^+) \equiv \sqrt{u_d^{+2} + w_d^{+2}} = 2.3$, shown in figure 6(*a*), distinctly visualize the time-averaged disc flow $\boldsymbol{u}_d$ as near-wall circular

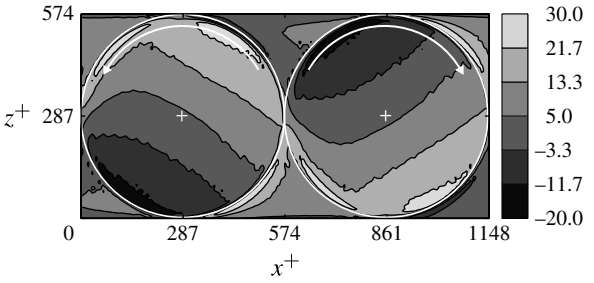

FIGURE 7. Contour plot of time-averaged streamwise wall friction $2\overline{\partial u/\partial y|}_{y=0}/(U_b^2 R_p)$ $(\times 10^3)$. The skin-friction coefficient is $C_f = 6.64 \times 10^{-3}$.

patterns of thickness of about $10\nu^*/u_\tau^*$. Well-defined, streamwise-elongated structures appear over sections of the stationary wall, where the shear brought about by the tangential disc flow is largest because discs which are next to each other along z have opposite sense of rotation. Figure 6(b) shows that these structures have a round shape when observed on the y–z plane at $x^+ = 0$, are centred at about $y^+ \approx 40$, and are higher than the ring-shaped patterns as they extend to about $y^+ \approx 80$.

Contour plots of u_d in x–z planes (not shown) reveal that for $y^+ > 15$ the discs engender spanwise-alternating streamwise bands of positive and negative u_d, i.e. of flow faster and slower than u_m respectively, showing that an interaction occurs between the two halves of the channel. The negative-u_d bands become wider and the positive-u_d bands become narrower as y increases. Figure 6(c) shows the bands in the centreline x–z plane. The wide positive-u_d bands are centred along lines parallel to x and passing through the disc centres, while the thinner and more energetic negative-u_d bands are centred along lines tangent to the discs.

Figure 7 shows the contour plot of the scaled time-averaged wall-normal gradient of the streamwise velocity at the wall, $2\overline{\partial u/\partial y|}_{y=0}/(U_b^2 R_p)$. The disc motion imposes a steady-wave pattern with a streamwise wavelength equal to $2D + 4c$. The wall forcing differs significantly from the one studied by Viotti *et al.* (2009). In the present case, the time-averaged streamwise wall-shear stress is spanwise dependent and negative over large portions of the disc, where the wall streamwise velocity attains large positive values near the disc tip. The absolute value of the maximum negative streamwise wall-shear stress ($\sim$0.02) is about three times larger than the spatial average, $C_f = 6.64 \times 10^{-3}$. In Viotti *et al.*'s case, the streamwise wall-shear stress is instead always positive and uniform along z.

3.3. *Turbulent flow visualizations and statistics*

Figure 8 shows instantaneous isosurfaces of $\mathrm{sgn}(u_t)q^+(u_t^+, w_t^+) = -3$ for stationary-wall (a) and disc-flow (b) conditions. The isosurfaces clearly visualize the low-speed streaks in the near-wall region. The intensity of these structures is reduced when they travel along the central part of the discs, whereas they are less affected when convecting over stationary-wall sections between discs.

Figure 9(a) presents the r.m.s. profiles of the components of $\boldsymbol{u}_d$ (henceforth the r.m.s. of a quantity a is defined as $a_{rms} \equiv \sqrt{\langle\overline{aa}\rangle}$). The $u_{d,rms}$ and $w_{d,rms}$ profiles reduce from the wall ($u^+_{d,rms}(0) = w^+_{d,rms}(0) = W^+\sqrt{(\pi/3)[1 + 2D^+/(2c^+ + D^+)]}/4 = 4.37$) and overlap when $y^+ < 10$, while $u_{d,rms} > w_{d,rms}$, $v_{d,rms}$ at higher locations. The $u_{d,rms}$ profile reaches a local minimum at $y^+ \approx 15$ ($u^+_{d,rms} \approx 1.2$) and a local maximum at $y^+ \approx 35$ ($u^+_{d,rms} \approx 1.5$). The minimum at $y^+ \approx 15$ is the cut-off between the region where the

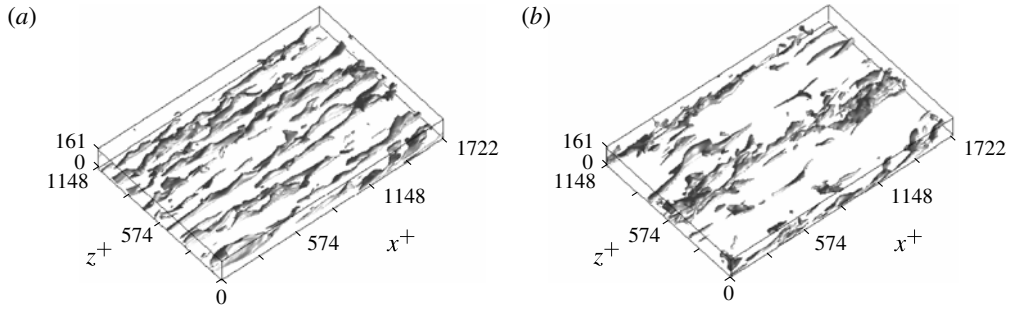

FIGURE 8. Isosurfaces of $\mathrm{sgn}(u_t)q(u_t^+, w_t^+) = -3$ for (*a*) stationary-wall and (*b*) disc-flow cases.

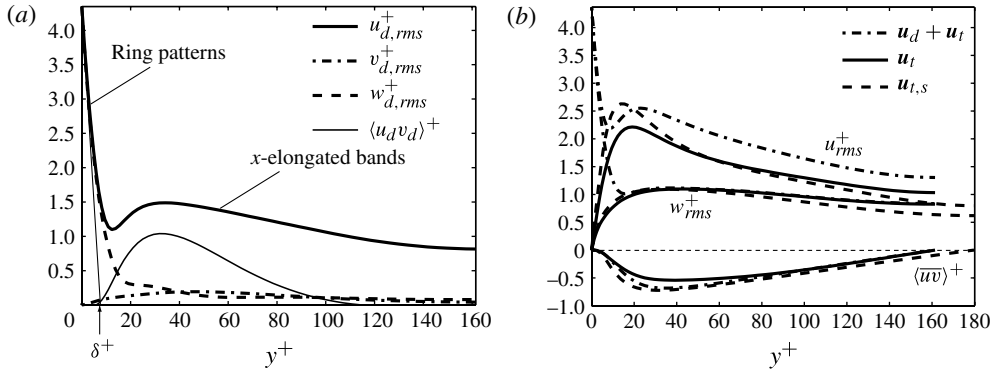

FIGURE 9. (*a*) Wall-normal profiles of r.m.s. of $\boldsymbol{u}_d$ components and of $\langle u_d v_d\rangle^+$ (the latter multiplied by a factor of 6); the disc-flow boundary layer thickness δ, defined in § 3.4, is shown. (*b*) Wall-normal profiles of r.m.s. of velocity components and Reynolds stresses.

disc-flow ring patterns exist near the wall and the region where the x-stretched bands appear at higher locations. The $w_{d,rms}$ profile drops up to $y^+ \approx 60$, and then it levels to $w^+_{d,rms} \approx 0.15$. It matches the $v_{d,rms}$ profile for $y^+ > 90$. Figure 9(*b*) shows the r.m.s. and Reynolds stresses $\langle \overline{uv}\rangle$ of $\boldsymbol{u}_d + \boldsymbol{u}_t$ (dash-dotted lines), $\boldsymbol{u}_t$ (solid lines), and $\boldsymbol{u}_{t,s}$ (dashed line). The intensity of the turbulent fluctuations and the Reynolds stresses is lower near the wall when compared with the stationary-wall case, as for the oscillating-wall case (Choi *et al.* 1998). The u_{rms} is affected the most as the peak is reduced by about 15% and shifts upward from $y^+ \approx 15$ to $y^+ \approx 20$. The $\langle \overline{uv}\rangle$ peak decreases by about 30%.

The FIK identity (Fukagata, Iwamoto & Kasagi 2002), adapted to account for the disc-flow effect (refer to appendix A), shows that the drag change is related to the disc-flow stresses $\langle u_d v_d\rangle$, shown in figure 9(*a*), and to the modification of the turbulent stresses, $\langle \overline{u_t v_t}\rangle - \langle \overline{u_{t,s} v_{t,s}}\rangle$, as follows:

$$\mathscr{R}\,(\%) = 100\frac{R_p \displaystyle\int_0^1 (1-y)[\langle \overline{u_t v_t}\rangle + \langle u_d v_d\rangle - \langle \overline{u_{t,s} v_{t,s}}\rangle]\,\mathrm{d}y}{U_b - R_p \displaystyle\int_0^1 (1-y)\langle \overline{u_{t,s} v_{t,s}}\rangle\,\mathrm{d}y}. \tag{3.1}$$

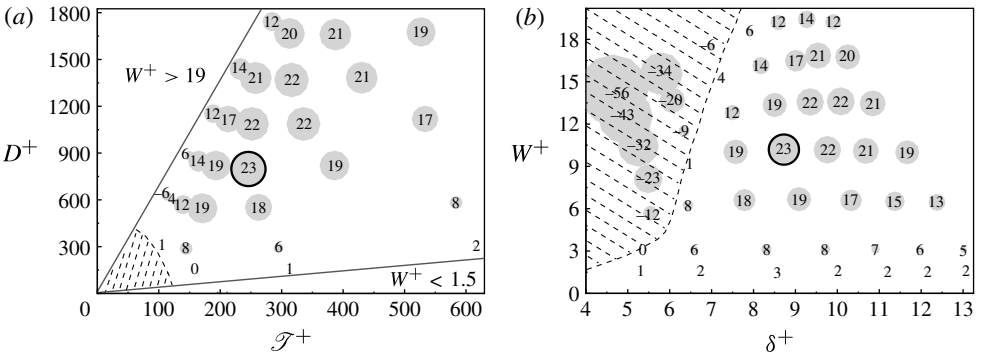

FIGURE 10. Map of (*a*) $\mathscr{R}(\mathscr{T}^+, D^+)$ (%) and (*b*) $\mathscr{R}(\delta^+, W^+)$ (%). The size of the grey circles is proportional to the absolute value of $\mathscr{R}$. The hatched areas denote drag-increase cases.

The drag reduction measured through (3.1) is $\mathscr{R} = 19.5\%$ for $D = 3.38$ and $W = 0.39$, which agrees with the value computed by the wall-shear stress, also $\mathscr{R} = 19.5\%$. The major contribution of $\langle u_d v_d \rangle$ comes from the x-stretched structures appearing between discs, shown in figure 6(*a,b*), while these stresses are of smaller magnitude over the discs. Along the dashed zero-$\mathscr{R}$ line in figure 4, both $\langle u_d v_d \rangle$ and $\langle \overline{u_t v_t} \rangle$ increase and balance each other as W grows, leaving the drag unchanged.

3.4. *Role of rotation period $\mathscr{T}$ and disc boundary layer thickness δ*

Figure 10(*a*) shows that the drag reduction reaches its maximum for a period of rotation $\mathscr{T}^+ = \pi D^+/W^+ = 2\pi/\Omega^+ \approx 246$ ($\mathscr{T} = 41$) and $D^+ = 801$ ($D = 5.07$). This characteristic time is about three times larger than the optimal period for the oscillating-wall technique, $T^+_{opt} \approx 75$ (Ricco *et al.* 2012). All the tested drag-increase cases (except $\mathscr{R} = -6.1\%$ for $D^+ = 626$, $\mathscr{T}^+ = 112$) cluster in the area marked by the hatching at small $\mathscr{T}^+$ and D^+. For $W^+ \leqslant 15$, this area is represented well by $(\mathscr{T}^+/a^+_{\mathscr{T}})^2 + (D^+/a^+_D)^2 < 1$, where $a^+_{\mathscr{T}} = 120$, $a^+_D = 480$. The condition for drag increase is therefore $W^+ > \pi D^+ a^+_D/[a^+_{\mathscr{T}}\,(a^{+2}_D - D^{+2})^{1/2}]$ for $W^+ \leqslant 15$.

Figure 10(*b*) shows $\mathscr{R}(\delta^+, W^+)$ (%), where δ is the disc-flow turbulent boundary layer thickness, defined as $\delta \equiv -[u_{d,rms}(0)/u'_{d,rms}(0) + w_{d,rms}(0)/w'_{d,rms}(0)]/2$, i.e. as the average of the y locations obtained by the interception of the tangents at the wall of the $u_{d,rms}$ and $w_{d,rms}$ profiles with the y axis (figure 9*a*). It is a measure of the wall-normal diffusion of the time-averaged viscous effects generated by the disc rotation. A minimum thickness is required for drag reduction; it increases from about $6\nu^*/u^*_\tau$ at $W^+ = 4$ to about $7.5\nu^*/u^*_\tau$ at $W^+ = 18$. The thickness $\delta^+ = 8.7$ corresponds to maximum drag reduction. These results are analogous to the travelling-wave technique (Quadrio & Ricco 2011), although for that case the viscous effects need to diffuse less from the wall, the minimum thickness being $\delta^+ = 1$ and the optimal thickness being $\delta^+ = 6.5$.

Figure 10(*b*) is also useful to compare the disc flow with steady-wave flow, studied by Viotti *et al.* (2009). As observed in figure 4, at a fixed D drag reduction increases with W up to an optimum, decreases, and then drag increase occurs. This behaviour is in sharp contrast with the corresponding one of Viotti *et al.* (2009)'s flow, for which $\mathscr{R}$ increases monotonically with W for a fixed forcing wavelength λ_x. In the disc-flow case, the initial growth of $\mathscr{R}$ with W occurs analogously to the steady-wave case

(although it is more gradual), but $\mathscr{R}$ eventually drops because the disc-flow boundary layer thickness becomes too thin to affect the near-wall turbulence effectively and to sustain the drag-reduction effect. In the steady-wave case, a good estimate is $\delta \sim \lambda_x^{1/3}$ (even in the turbulent flow case) and therefore the detrimental mismatch between the wall-normal scales of the wall turbulence and the generalized boundary layer thickness does not occur as W grows. The two techniques also present different drag-reduction dependences on D at fixed W. An optimum forcing streamwise length scale exists in both cases. However, in the disc case, the optimum D grows with W from $D^+ = 600$ as $W^+ \to 0$ to $D^+ = 1500$ when $W^+ \approx 20$, as shown by the black dots in figure 4(*b*), whereas, in the steady-wave case, the optimum wavelength is approximately constant, $\lambda_x^+ \approx 1000$–1250, as the maximum wall velocity increases to $W^+ = 12$. Furthermore, while the disc flow exhibits large drag increase at small D, Viotti *et al.* (2009) report drag reduction at small λ_x.

3.5. *Power spent on disc motion, net power saved, and power gain*

As the disc-flow technique is active, power is supplied to the system for rotating the discs against the viscous resistance of the fluid. The power $\mathscr{P}_{sp,t}\,(\%)$ is the percentage of the power spent $\mathscr{W}$ to move the discs with respect to the power $\mathscr{P}_x$ employed to drive the fluid along the streamwise direction in the stationary-wall case, i.e.

$$\begin{aligned}\mathscr{P}_{sp,t}\,(\%) \equiv \frac{100\mathscr{W}}{\mathscr{P}_x} &= -\frac{100R_p}{R_{\tau,s}^2 U_b}\left\langle u_d(x,0,z)\left.\frac{\partial u_d}{\partial y}\right|_{y=0} + w_d(x,0,z)\left.\frac{\partial w_d}{\partial y}\right|_{y=0}\right\rangle \\ &= -\frac{100R_p}{2R_{\tau,s}^2 U_b}\left.\frac{\mathrm{d}\left(u_{d,rms}^2 + w_{d,rms}^2\right)}{\mathrm{d}y}\right|_{y=0}, \end{aligned} \tag{3.2}$$

which are found from the viscous work term in the kinetic energy equation (1–108) on page 71 in Hinze (1975) (refer to appendix B). Through the definition of δ in § 3.4 and by assuming $u'_{d,rms}(0) \approx w'_{d,rms}(0)$ as suggested by figure 9(*a*), (3.2) can be simplified to $\mathscr{P}_{sp,t}\,(\%) \approx 25\pi W^2 R_p/(2\delta U_b R_{\tau,s}^2)$.

Figure 11(*a*) depicts $\mathscr{P}_{sp,t}\,(\%)$ versus $\mathscr{P}_{sp,l}\,(\%)$, which is computed through the solution of the laminar flow induced by an infinite disc rotating beneath a still fluid, i.e. $\mathscr{P}_{sp,l}\,(\%) = -100GW^{5/2}R_p^{3/2}/(\sqrt{2D}U_b R_{\tau,s}^2)$, where $G = -0.61592$ (Rogers & Lance 1960). This formula is also useful to compute the power spent in rotating a disc below a laminar flow with uniform shear (Wang 1989). The laminar power spent $\mathscr{P}_{sp,l}$ predicts $\mathscr{P}_{sp,t}$ well for $\mathscr{P}_{sp,t}$ up to about 25%. The agreement at low power is expected because W is small when $\mathscr{P}_{sp,t}$ is small and therefore the infinite-disc approximation is satisfactory because the interaction between the radial flows produced by neighbouring discs is negligible. Similarly to the travelling-wave case (Quadrio & Ricco 2011), the laminar flow is instrumental in the computation of the power spent.

The time-averaged power per unit area spent to activate the discs is also studied:

$$\begin{aligned} w(x,z) &\equiv \frac{1}{R_p}\overline{u_i\left(\frac{\partial u_i}{\partial x_j} + \frac{\partial u_j}{\partial x_i}\right)} \\ &= \frac{1}{R_p}\left[u_d(x,0,z)\left(u'_m(0) + \left.\frac{\partial u_d}{\partial y}\right|_{y=0}\right) + w_d(x,0,z)\left.\frac{\partial w_d}{\partial y}\right|_{y=0}\right], \end{aligned} \tag{3.3}$$

which is related to the total power employed to move the discs, $\mathscr{W} = 2L_x L_z \langle w \rangle$ (refer to appendix B). Comparing (3.3) and (B 5) shows that $u'_m(0)$, the mean wall-normal

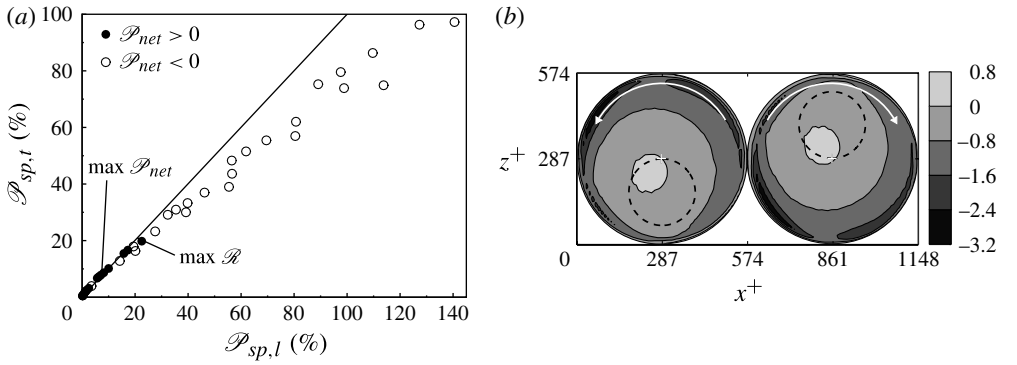

FIGURE 11. (*a*) $\mathscr{P}_{sp,t}$ (%), computed through (3.2), versus $\mathscr{P}_{sp,l}$ (%), obtained from the laminar solution of the flow induced by an infinite disc rotating beneath a still fluid. (*b*) Contour plot of $w(x^+, z^+)$ ($\times 10^3$), time-averaged power per unit area spent to activate the discs, defined in (3.3). The dashed lines, computed through the laminar-flow inequality (C 2), denote the predicted regions of disc surface where $w > 0$.

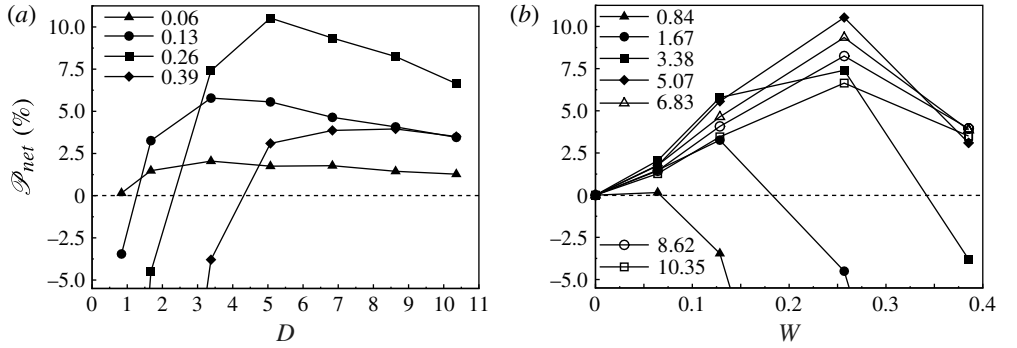

FIGURE 12. (*a*) $\mathscr{P}_{net}(D; W)$ (%); the values of W are given in the legend. (*b*) $\mathscr{P}_{net}(W; D)$ (%); the values of D are given in the legend.

gradient of the streamwise velocity at the wall, only has an effect on the local power w, and not on the space-averaged power $\mathscr{W}$. Figure 11(*b*) shows the contour plot of w. The round region near the disc centre corresponds to positive w, i.e. the fluid exerts work on the disc, while w is negative over most of the disc surface, i.e. where energy is supplied to the fluid. This is a case of spatially localized regenerative braking effect, which has a temporal analogue in the oscillating-wall technique. For this latter flow, the space-averaged power may be positive or negative during the temporal cycle. The dashed lines enclose areas over the disc surface where $w > 0$ as predicted by the laminar flow generated by an infinite spinning disc (refer to appendix C). Although larger than the regions obtained via direct numerical simulations, their round shape and location (confined to $u_d(y = 0) > 0$) are satisfactorily predicted.

Another quantity of interest is the net power saved $\mathscr{P}_{net}$, defined as the difference between the power saved thanks to the wall motion, which coincides with drag reduction at constant mass flow rate, and the power spent $\mathscr{P}_{sp,t}$, i.e. $\mathscr{P}_{net}$ (%) $\equiv \mathscr{R}$ (%) $- \mathscr{P}_{sp,t}$ (%). The graphs in figure 12 and the map at the top of figure 4 (boxed numbers) show that a positive $\mathscr{P}_{net}$ may occur for $W \leqslant 0.39$

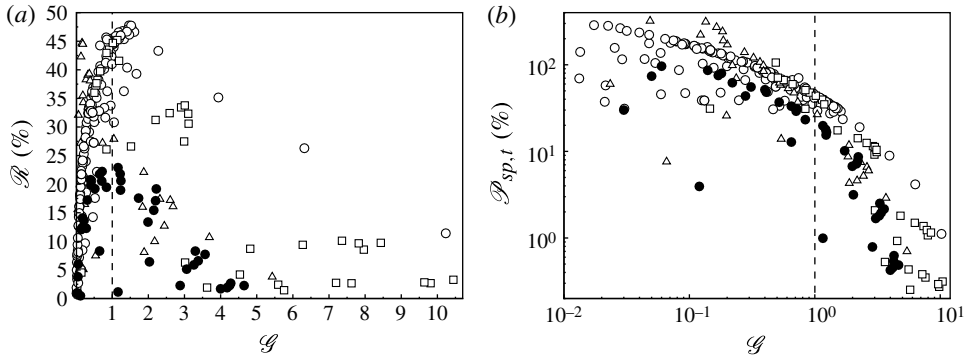

FIGURE 13. (*a*) $\mathscr{R}$ (%) versus $\mathscr{G}$ and (*b*) $\mathscr{P}_{sp,t}$ (%) versus $\mathscr{G}$. The black circles indicate disc-flow data, the white circles the travelling-wave data by Quadrio *et al.* (2009), the squares the steady-wave data by Viotti *et al.* (2009), and the triangles the oscillating-wall data by Quadrio & Ricco (2004).

and a maximum $\mathscr{P}_{net} = 10.5\%$ is computed for $D = 5.07$ and $W = 0.26$ ($D^+ = 820$, $W^+ = 6.7$, $\mathscr{T}^+ = 386$, $\delta^+ = 9.1$, $\mathscr{R} = 19.2\%$). The threshold diameter above which $\mathscr{P}_{net}$ is positive increases with W. The power $\mathscr{P}_{net}$ grows negative for small D and large W because both the drag and $\mathscr{P}_{sp,t}$ increase significantly. Figure 11(*a*) also shows that the power spent for the positive-$\mathscr{P}_{net}$ cases (which include the maximum-$\mathscr{R}$ case) is computed through the laminar flow solution more accurately than for the negative-$\mathscr{P}_{net}$ cases. The optimum $W^+ = 6.7$ for maximum $\mathscr{P}_{net}$ is comparable with the one for the steady-wave case studied by Viotti *et al.* (2009), $W^+ = 5.3$, while the optimum forcing streamwise length scales differ approximately by a factor of two, i.e. $D^+ = 820$ and $\lambda_x^+ = 870$ in Viotti *et al.*'s case.

The power gain, defined as $\mathscr{G} \equiv \mathscr{R}/\mathscr{P}_{sp,t}$ (Iwamoto, Suzuki & Kasagi 2002), is another useful parameter for assessing the performance of a drag-reduction technique. Its values are reported in table 5. Figure 13(*a*) shows that the maximum $\mathscr{R}$ achieved by the rotating discs is about half of that achieved by the travelling waves, studied by Quadrio, Ricco & Viotti (2009), or by the oscillating-wall technique (Quadrio & Ricco 2004). The $\mathscr{G}$ values for maximum $\mathscr{R}$ for the discs and the waves are comparable, $\mathscr{G} \approx 1.25$ and 1.6 respectively, and higher than the ones for the oscillating-wall flow, $\mathscr{G} \approx 0.16$. In the tested parameter range, the discs may offer $\mathscr{G}$ values which are comparable with the ones of the oscillating-wall technique. It is further noted that large disc-flow gain values (the largest being $\mathscr{G} = 4.5\%$) correspond to low $\mathscr{R}$. Figure 13(*b*) shows that, although the waves perform better in terms of maximum gain values, the power spent in rotating the discs may be lower than that needed by the steady or travelling waves to obtain the same $\mathscr{G} > 1$ values. It should be noted that the steady or travelling waves may offer even higher values for maximum $\mathscr{R}$ and maximum $\mathscr{G}$ because the full space of the forcing parameters has not been explored yet.

4. Outlook for the future

Table 6 presents estimated data for low-speed laboratory conditions and for three flows of technological interest for disc-flow parameters leading to $\mathscr{R} = 20\%$. They are found through the empirical correlations given in the table caption. These values can be a useful guide for practical implementations. Wind tunnel and water channel

Quantity	Flight (BL)	Ship (BL)	Train (BL)	WT (BL)	WC (BL)	WC (CF)
U^* (m s^{-1})	225	10	83	11.6	0.37	0.28
$\nu^* \times 10^6$ (m^2 s^{-1})	35.3	1.52	15.7	15.7	1	1
x^* (m)	1.5	1.45	1.8	1	2	—
h^* (mm)	22.3	21.6	26.8	24.8	49.6	10
$u^*_{\tau,s}$ (m s^{-1})	7.9	0.35	2.9	0.51	0.02	0.02
$R_{\tau,s}$	4970	4970	4970	800	800	180
$C_{f,s} \times 10^3$	2.44	2.44	2.44	3.82	3.82	8.14
D^* (mm)	6.7	6.5	8.1	46.5	93	83.5
W^* (m s^{-1})	78.6	3.5	29	5.1	0.16	0.18
f^* (Hz)	3718	170	1138	34.6	0.55	0.68
δ^* (μm)	39	38	47	270	540	480
$\boldsymbol{T}^*$ (μNm)	6	35	6	55	380	230
$\mathscr{P}_{sp,t}{}^*$ (mW)-one disc	140	40	40	12	1.3	1

TABLE 6. Dimensional quantities for typical conditions of turbulent boundary layers with no pressure gradient (BL) and pressure-driven channel flows (CF) (WT stands for wind tunnel and WC for water channel). Top seven rows: Stationary-wall conditions; U^* indicates the free-stream mean velocity for BLs and U_b^* for CF, x^* is the downstream location, $h^* = 0.37x^*\,(x^*U^*/\nu^*)^{-0.2}$ denotes the BL thickness, and $C_f = 0.0336R_\tau^{-0.273}$ for CF and $C_f = 0.37\,[\log_{10}(x^*U^*/\nu^*)]^{-2.584}$ for BLs (Pope 2000). Flight conditions are at 10 km above sea level. Bottom six rows: Disc-flow parameters for $D^+ = 1500$, $W^+ = 10$ ($\mathscr{R} = 20\%$). $\boldsymbol{T}^*$ indicates the torque.

experiments may be realizable with contained costs as the diameter is of the order of 5–10 cm and the rotational frequency is about 35 Hz in air and less than 1 Hz in water (for $R_\tau = 800$ for free-stream boundary layers and $R_\tau = 180$ for channel flow).

The predicted quantities in flight conditions also look promising, as the diameter is about 6.7 mm, the tip velocity is about 80 m s^{-1}, and the rotational frequency is about 3700 Hz. A lower rotational frequency of 2230 Hz at the same diameter ($W^* = 50$ m s^{-1}, $W^+ = 6.5$) guarantees $\mathscr{P}_{net} = 8\%$. These estimates are more optimistic for future implementations than the ones put forward by Keefe (1997). For flight conditions, the diameter in table 6 is about two orders of magnitude larger than the one suggested by Keefe ($D^* = 80$–90 μm, $D^+ = 20$) and the frequency is one order of magnitude smaller than Keefe's ($f^* = 72$ kHz, $\mathscr{T}^+ = 20$). The reason for these disagreements lies in Keefe's estimates being based on untested physical hypotheses, i.e. the diameter being smaller than the streak spacing along the spanwise direction, about $100\nu^*/u^*_\tau$, and the frequency being comparable with the peak of the fluctuating normal vorticity at $y^+ \approx 10$. Keefe's figures may lead to drag increase as his proposed case falls within the hatched area in figure 10(*a*).

The disc-flow parameters for turbulent flows over hulls of large-scale ships and over high-speed trains at the same flight-condition R_τ are also of interest. The values of the disc diameter are similar to the ones in flight conditions ($D^* = 6.5$ mm for ships and $D^* = 8.1$ mm for trains), but the advantage is in the lower rotational rates, i.e. $W^* = 3.5$ m s^{-1} and $f^* = 170$ Hz for ships, and $W^* = 29$ m s^{-1} and about $f^* = 1140$ Hz for trains. Figure 14 shows typical spatial and temporal scales of turbulent coherent structures (Kasagi, Suzuki & Fukagata 2009) and the corresponding disc diameters and periods of rotation for the above-mentioned flows of technological

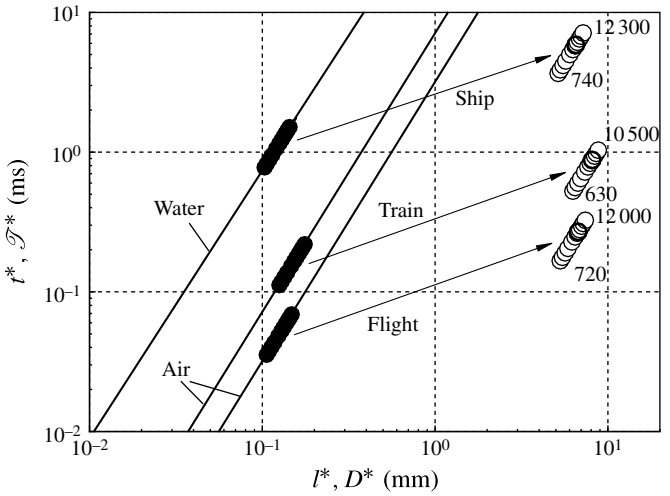

FIGURE 14. Spatial scales l^* and temporal scales t^* of near-wall vortical structures for $l^+ = 30$ and $t^+ = 100$ for flows over aircraft ($U^* = 225$ m s^{-1}), ship hulls ($U^* = 10$ m s^{-1}), and high-speed trains ($U^* = 83$ m s^{-1}) in the range 0.1 m $\leqslant x^* \leqslant$ 5 m (black circles), adapted from Kasagi *et al.* (2009). The disc diameters D^* and periods of rotation $\mathscr{T}^*$, indicated by white circles, are for $D^+ = 1500$ and $\mathscr{T}^+ = 470$. The numbers denote the values of R_τ and the thicker circles denote the cases presented in table 6.

interest. For an extended R_τ range and for all three cases, the disc diameter is almost two orders of magnitude larger than the length scale of the vortices and the period of rotation is almost one order of magnitude larger than the time scale of the near-wall turbulence. This renders the discs attractive compared to presently studied feedback-control actuators, which are thought to operate optimally at spatio-temporal scales comparable with the ones of the near-wall turbulence (Yoshino, Suzuki & Kasagi 2008). These results prove that forcing the near-wall turbulence at a scale which is much larger than that of the near-wall vortices (the optimal diameter is about five times the half channel height) is an effective method for drag reduction. This is in line with the works by Willis *et al.* (2010) and Sharma *et al.* (2011), which indicate that a near-wall body-force controller is most potent when acting on low-wavenumber structures.

Rotation rates of $O(10^3)$ Hz may be obtained by commercially available electromagnetic motors which can be as small as 2 mm in diameter (Kuang-Chen Liu, Friend & Yeo 2010). The micromachined air turbine developed for the first time by Frechette *et al.* (2005), supported by gas-lubricated bearings and consisting of a single-stage radial inflow, may represent another solution for the implementation of the discs. The turbine has a rotor diameter of 4.2 mm and can operate at a maximum tip speed of 300 m s^{-1} (maximum frequency of 17 kHz) with an isentropic efficiency of 87%. It can exert a maximum torque of 30 μNm and supply a maximum mechanical power of 5 W. The flight-condition values in table 6 may be achieved by this technology.

The discs may offer some advantages over passive drag-reduction techniques, such as riblets and compliant surfaces, which, despite about thirty years of research, have never been utilized in technological flow systems and have never led to amounts of drag reduction higher than 10% (Gad-el Hak 2002). Differently from compliant

surfaces, the discs are rigid and therefore more resistant to wear due to use. Their motion and size can be relatively easily adjusted to the boundary layer growth and they may offer more possibilities for optimized forcing conditions and controlled parametric studies than passive methods. The main advantage over suction/blowing techniques is the absence of fluid exchange through the surface. In case of failure, the rotating discs would not lead to off-design drag increase, as for compliant surfaces because of undesired changes of mechanical properties, or for suction and ribbed surfaces because of dirt deposition, caused in the latter case by the very small maximum riblet height in flight conditions, about 0.15 mm (Viswanath 2002).

In spite of these advantages, there are major challenges related to the technological implementation of the discs. The complexity of the design, the increase of weight, the achievement of a positive net energy balance when electrical and mechanical losses are taken into account, the influence of fatigue and frictional wearing on the long-term reliability of the system, the difficulties related to repair of faulty parts, and the functionality of the discs in adverse environmental conditions are undoubtedly serious issues that would have to be considered. For commercial aircraft cruising at high-Mach-number subsonic conditions, the shear flow induced between discs may reach supersonic speed, giving rise to intense aerothermodynamic heating.

The influence of R_τ cannot be accounted for at this stage. Recent studies on spanwise wall forcing, by Gatti (2011) from Quadrio's group and Touber & Leschziner (2012), suggest that the optimal forcing parameters remain largely unchanged as R_τ increases, while the drag reduction may drop as $\sim R_\tau^{-\alpha}$ (α in the range 0.007–0.22), i.e. $\mathscr{R} = 40\%$ may decrease to $\mathscr{R} = 25\%$ at $R_\tau = 5000$. The power spent $\mathscr{P}_{sp,t}$ is predicted to drop as $\sim R_\tau^{-0.19}$, which indicates that the R_τ effect on $\mathscr{P}_{net}$ may be less significant than on the drag reduction.

The experimental verification of our simulations and studies on the effects of the flow geometry (free stream versus confined flows) and compressibility are other priorities in view of future applications. It is to be investigated how such variations impinge on the drag reduction and the net power saved, on the optimal tip velocity and diameter, and on the predicted values in table 6 and in figure 14. Despite the complexity of this technique, it is our hope that the present results will spur further interest towards active forcing of wall turbulence by wall-normal vorticity, as opposed to the widely studied suction–blowing actuation. As foreseen by Keefe (1998), the possibilities of improvement, in terms of drag reduction, net power saved, separation control, enhancement of heat transfer and lift, may be broad and interesting.

Acknowledgements

We would like to thank the referees for the useful comments. P.R. was partly supported by EPSRC First Grant *EP/I033173/1*. The help from Dr A. Brookfield at the University of Sheffield on computational issues is gratefully acknowledged. We thank Mr D. Wise for the interesting discussions and for implementing the parallel version of the code, and Dr M. Seddighi and Professor S. He for the exchange of ideas and for running their finite-difference code. We are indebted to Drs R. J. Poole and M. W. Johnson at the University of Liverpool for the incisive comments on the advantages of the discs over other drag-reduction techniques. We also thank Drs P. Hicks, A. Willis, R. Howell, A. Marzo, A. Sharma, C. Keylock, F. Nicolleau, and Professor K. Worden for their input and encouragement, and Professor D. G. Bogard at the University of Texas at Austin for suggesting this problem. We also acknowledge the interesting discussions with Drs S. Rolston and R. Ashworth from EADS Innovation Works UK.

Appendix A. Derivation of Fukagata–Iwamoto–Kasagi identity (3.1) for disc flow

The FIK identity for the disc flow is obtained through a straightforward extension of the original identity discovered by Fukagata *et al.* (2002) (FIK). Consider first the streamwise momentum equation:

$$\frac{\partial u}{\partial t}+\frac{\partial (uu)}{\partial x}+\frac{\partial (uv)}{\partial y}+\frac{\partial (uw)}{\partial z}=-\frac{\partial p}{\partial x}+\frac{1}{R_p}\left(\frac{\partial^2 u}{\partial x^2}+\frac{\partial^2 u}{\partial y^2}+\frac{\partial^2 u}{\partial z^2}\right). \tag{A 1}$$

By inserting the velocity decomposition introduced in § 2 and the analogous pressure decomposition $p=p_m+p_d+p_t$ in (A 1), by averaging in time, along x and z, and over the two channel halves, it follows that:

$$-\frac{\mathrm{d}p_m}{\mathrm{d}x}=\frac{1}{R_p}\frac{\partial}{\partial y}\left[\langle\overline{u_t v_t}\rangle+\langle u_d v_d\rangle-\frac{\partial u_m}{\partial y}\right]. \tag{A 2}$$

Equation (A 2) is analogous to equation (1) in FIK: the only difference resides in the additional disc-flow Reynolds stress term $\langle u_d v_d\rangle$ (the last two terms in equation (1) in that paper are null here because the time-averaged mean flow is statistically homogeneous along x). The procedure which follows is therefore exactly the same as in FIK if the Reynolds stress term in equation (1) in FIK is replaced by $\langle\overline{u_t v_t}\rangle+\langle u_d v_d\rangle$. It is found that

$$C_f=\frac{6}{U_b R_p}-\frac{6}{U_b^2}\int_0^1 (1-y)\left[\langle\overline{u_t v_t}\rangle+\langle u_d v_d\rangle\right]\mathrm{d}y. \tag{A 3}$$

As $\mathscr{R}\,(\%)=100(C_{f,s}-C_f)/C_{f,s}$, formula (3.1) is obtained.

Appendix B. Derivation of formula (3.2) for power spent on disc motion

The work $\mathscr{W}$ done by the viscous stresses per unit time within the volume $L_x\times L_y\times L_z$ is found by the volume integral of term III in equation (1–108) on page 71 in Hinze (1975) for the kinetic energy balance for the incompressible flow of a Newtonian fluid, i.e.

$$\mathscr{W}=\frac{L_x L_z}{R_p}\left\langle\int_0^2\frac{\partial}{\partial x_j}\left[u_i\left(\frac{\partial u_i}{\partial x_j}+\frac{\partial u_j}{\partial x_i}\right)\right]\mathrm{d}y\right\rangle, \tag{B 1}$$

where the Einstein summation convention of repeated indices is adopted and the subscripts $i=1,2,3$ denote the x,y,z directions and the corresponding velocity components. Formula (B 1) simplifies to

$$\mathscr{W}=\frac{L_x L_z}{R_p}\left\langle\int_0^2\frac{\partial}{\partial y}\left[u\left(\frac{\partial u}{\partial y}+\frac{\partial v}{\partial x}\right)+2v\frac{\partial v}{\partial y}+w\left(\frac{\partial w}{\partial y}+\frac{\partial v}{\partial z}\right)\right]\mathrm{d}y\right\rangle \tag{B 2}$$

through integration over x–z planes because of periodicity along x and z. By integration along y, formula (B 2) reduces to

$$\mathscr{W}=\frac{L_x L_z}{R_p}\left\langle u(y=0)\left.\frac{\partial u}{\partial y}\right|_{y=0}+w(y=0)\left.\frac{\partial w}{\partial y}\right|_{y=0}+u(y=2)\left.\frac{\partial u}{\partial y}\right|_{y=2}+w(y=2)\left.\frac{\partial w}{\partial y}\right|_{y=2}\right\rangle, \tag{B 3}$$

because $v(y=0)=v(y=2)=0$. By substituting the velocity decomposition given at the end of § 2 and noting that $u(y=0)=u(y=2)=u_d(x,0,z)$ and $w(y=0)=u(y=2)=w_d(x,0,z)$, formula (B 3) becomes

$$\mathscr{W}=\frac{L_xL_z}{R_p}\left\langle u_d(x,0,z)\left(\left.\frac{\partial u_d}{\partial y}\right|_{y=0}+\left.\frac{\partial u_t}{\partial y}\right|_{y=0}+\left.\frac{\partial u_d}{\partial y}\right|_{y=2}+\left.\frac{\partial u_t}{\partial y}\right|_{y=2}\right)\right.$$
$$\left.+\ w_d(x,0,z)\left(\left.\frac{\partial w_d}{\partial y}\right|_{y=0}+\left.\frac{\partial w_t}{\partial y}\right|_{y=0}+\left.\frac{\partial w_d}{\partial y}\right|_{y=2}+\left.\frac{\partial w_t}{\partial y}\right|_{y=2}\right)\right\rangle, \tag{B 4}$$

because $u'_m(0)$ and $u'_m(2)$ are constants and $\langle u_d(x,0,z)\rangle=\langle w_d(x,0,z)\rangle$=0. Averaging (B 4) in time and over the two channel walls leads to

$$\mathscr{W}=\frac{2L_xL_z}{R_p}\left\langle u_d(x,0,z)\left.\frac{\partial u_d}{\partial y}\right|_{y=0}+w_d(x,0,z)\left.\frac{\partial w_d}{\partial y}\right|_{y=0}\right\rangle \tag{B 5}$$

because $\overline{u_t}=\overline{w_t}=0$. The work $\mathscr{W}$ is the power employed to move the discs against the viscous resistance of the fluid.

The other quantity of interest is $\mathscr{P}_x$, the time-averaged volume integral of the power used to drive the fluid along the streamwise direction in the stationary-wall case (refer to the first term on the right-hand side of the first equation (1–108) in Hinze 1975), which reads

$$\mathscr{P}_x=L_xL_z\left\langle\int_0^1\overline{u\frac{\partial p}{\partial x}}+\overline{v\frac{\partial p}{\partial y}}+\overline{w\frac{\partial p}{\partial z}}\mathrm{d}y\right\rangle. \tag{B 6}$$

By substituting the velocity decomposition introduced in § 2 and the pressure decomposition given in appendix A, formula (B 6) simplifies to

$$\mathscr{P}_x=L_xL_z\left[\frac{\mathrm{d}p_m}{\mathrm{d}x}\int_0^1 u_m(y)\mathrm{d}y+\left\langle\int_0^1\overline{u_{i,d}\frac{\partial p_d}{\partial x_i}}+\overline{u_{i,t}\frac{\partial p_t}{\partial x_i}}\mathrm{d}y\right\rangle\right], \tag{B 7}$$

because $\overline{u_t}=\overline{v_t}=\overline{w_t}=\overline{p_t}=0$ and $\mathrm{d}p_m/\mathrm{d}x$ is spatially uniform. The x–z-integrated term in (B 7) is shown to be null by use of the continuity equation and because of periodicity along x and z. By use of (2.3), on noting that $\mathrm{d}p_m/\mathrm{d}x=-u'_m(0)/R_p$ (found by integrating (A 2) along y) and $u'_m(0)=R^2_{\tau,s}/R_p$, it follows that

$$\mathscr{P}_x=-2U_bL_xL_z\left(\frac{R_{\tau,s}}{R_p}\right)^2. \tag{B 8}$$

The percentage power required to move the discs is defined as $\mathscr{P}_{sp,t}\,(\%)=100\mathscr{W}/\mathscr{P}_x$. Substitution of (B 5) and (B 8) into the latter gives the first formula in (3.2). By noting that $u_d(x,0,z)\partial u_d/\partial y|_{y=0}=0.5\partial u_d^2/\partial y|_{y=0}$ and $u^2_{d,rms}=\langle u_d^2\rangle$, the second formula in (3.2) is obtained.

Appendix C. Estimation of time-averaged power spent w through solution of laminar flow induced by an infinite spinning disc

The time-averaged local power $w(x,z)$ spent to move the discs (given in (3.3)) can be estimated through the solution of the laminar flow induced by an infinite disc rotating below a still fluid (Rogers & Lance 1960). The streamwise and spanwise components of the disc flow can be expressed as $u_d=w_r\cos(\theta)$ and $w_d=-w_r\sin(\theta)$, respectively, where w_r is the laminar tangential velocity component and θ is the angle

in the cylindrical coordinate system with origin located at the centre of the disc. By writing $w_r(y=0) = 2Wr/D$ and $\partial w_r/\partial y|_{y=0} = rGR_p^{1/2}\,(2W/D)^{3/2}$, (3.3) becomes

$$w = \frac{2Wr}{DR_p}\left[u'_m(0)\cos(\theta) + rGR_p^{1/2}\left(\frac{2W}{D}\right)^{3/2}\right]. \tag{C 1}$$

The contribution of the disc flow $\boldsymbol{u}_d$ to w, given by the right-hand term in (C 1), is always negative because $G < 0$. The mean-flow gradient at the wall, $u'_m(0)$, may cause w to be positive and only when $\cos(\theta) > 0$. For the disc on the left of figure 11(*b*), the condition $w > 0$ translates to

$$\left.\begin{aligned} &(2x^+ - \hat{D}^+)^2 < (\hat{D}^+ - 2z^+)(\gamma - \hat{D}^+ + 2z^+), \\ &\hat{D} = D + 2c, \quad \gamma = \frac{-2u'_m(0)R_\tau}{GR_p^{1/2}}\left(\frac{D}{2W}\right)^{3/2}. \end{aligned}\right\} \tag{C 2}$$

It is clear that the region of positive w, indicated by the dashed lines in figure 11(*b*), becomes smaller as W grows.

REFERENCES

ASCHER, U. M., RUUTH, S. J. & WETTON, B. T. R. 1995 Implicit-explicit methods for time-dependent partial differential equations. *SIAM J. Numer. Anal.* **32**, 797–823.

AUTERI, F., BARON, A., BELAN, M., CAMPANARDI, G. & QUADRIO, M. 2010 Experimental assessment of turbulent drag reduction by travelling waves in a turbulent pipe flow. *Phys. Fluids* **22**, 115103/14.

CANUTO, C., HUSSAINI, M. Y., QUARTERONI, A. & ZANG, T. A. 1988 *Spectral Methods in Fluid Dynamics*. Springer.

CHOI, K.-S. 2002 Near-wall structure of turbulent boundary layer with spanwise-wall oscillation. *Phys. Fluids* **14** (7), 2530–2542.

CHOI, K.-S. & CLAYTON, B. R. 2001 The mechanism of turbulent drag reduction with wall oscillation. *Intl J. Heat Fluid Flow* **22**, 1–9.

CHOI, K.-S., DEBISSCHOP, J. R. & CLAYTON, B. R. 1998 Turbulent boundary-layer control by means of spanwise-wall oscillation. *AIAA J.* **36** (7), 1157–1162.

DHANAK, M. R. & SI, C. 1999 On reduction of turbulent wall friction through spanwise oscillations. *J. Fluid Mech.* **383**, 175–195.

DUQUE-DAZA, C. A., BAIG, M. F., LOCKERBY, D. A., CHERNYSHENKO, S. I. & DAVIES, C. 2012 Modelling turbulent skin-friction control using linearized Navier-Stokes equations. *J. Fluid Mech.* **702**, 403–414.

FRECHETTE, L. G., JACOBSON, S. A., BREUER, K. S., EHRICH, F. F., GHODSSI, R., KHANNA, R., WONG, C. W., ZHANG, X., SCHMIDT, M. A. & EPSTEIN, A. H. 2005 High-speed microfabricated silicon turbomachinery and fluid film bearings. *J. Microel. Sys.* **14** (1), 141–152.

FUKAGATA, K., IWAMOTO, K. & KASAGI, N. 2002 Contribution of Reynolds stress distribution to the skin friction in wall-bounded flows. *Phys. Fluids* **14** (11), 73–76.

GAD-EL HAK, M. 2002 Compliant coatings for drag reduction. *Prog. Aerosp. Sci.* **38**, 77–99.

GATTI, D. 2011 Turbulent drag reduction at moderate Reynolds number via spanwise velocity waves. Master's thesis, Politecnico di Milano.

GIBSON, J. F. 2006 Channelflow: a spectral Navier-Stokes simulator in C++. http://www.channelflow.org/.

GIBSON, J. F., HALCROW, J. & CVITANOVIC, P. 2008 Visualizing the geometry of state space in plane Couette flow. *J. Fluid Mech.* **611**, 107–130.

GOUDER, K., POTTER, M. & MORRISON, J. F. 2013 Turbulent friction drag reduction using electroactive polymer and electromagnetically driven surfaces. *Exp. Fluids* **54**, 1–12.

HINZE, J. O. 1975 *Turbulence*, 2nd edn. McGraw Hill.

IWAMOTO, K., SUZUKI, Y. & KASAGI, N. 2002 Reynolds number effect on wall turbulence: toward effective feedback control. *Intl J. Heat Fluid Flow* **14** (11), 73–76.

JUNG, W. J., MANGIAVACCHI, N. & AKHAVAN, R. 1992 Suppression of turbulence in wall-bounded flows by high-frequency spanwise oscillations. *Phys. Fluids* A **4** (8), 1605–1607.

KANNEPALLI, C. & PIOMELLI, U. 2000 Large-eddy simulation of a three-dimensional shear-driven turbulent boundary layer. *J. Fluid Mech.* **423**, 175–203.

KASAGI, N., SUZUKI, Y. & FUKAGATA, K. 2009 Micromechanical systems-based feedback control of turbulence for skin friction reduction. *Annu. Rev. Fluid Mech.* **41**, 231–251.

KEEFE, L. 1997 A normal vorticity actuator for near-wall modification of turbulent shear flows. *AIAA Paper* 97-0547.

KEEFE, L. 1998 Method and apparatus for reducing the drag of flows over surfaces. *United States Patent* 5,803,409.

KIM, J., MOIN, P. & MOSER, R. 1987 Turbulence statistics in fully developed channel flow at low Reynolds number. *J. Fluid Mech.* **177**, 133–166.

KLEISER, L. & SCHUMANN, U. 1980 Treatment of incompressibility and boundary conditions in 3-D numerical spectral simulations of plane channel flows. In *Proceedings of 3rd GAMM Conference Numerical Methods in Fluid Mechanics* (ed. E. Hirschel), pp. 165–173. GAMM, Vieweg.

KUANG-CHEN LIU, D., FRIEND, J. & YEO, L. 2010 A brief review of actuation at the micro-scale using electrostatics, electromagnetics and piezoelectric ultrasonics. *Acoust. Sci. Tech.* **31**, 115–123.

LESIEUR, M. 1997 *Turbulence in Fluids*, 3rd edn. Kluwer.

MOARREF, R. & JOVANOVIC, M. R. 2012 Model-based design of transverse wall oscillations for turbulent drag reduction. *J. Fluid Mech.* **707**, 205–240.

POPE, S. B. 2000 *Turbulent Flows*. Cambridge University Press.

QUADRIO, M. & RICCO, P. 2004 Critical assessment of turbulent drag reduction through spanwise wall oscillations. *J. Fluid Mech.* **521**, 251–271.

QUADRIO, M. & RICCO, P. 2011 The laminar generalized Stokes layer and turbulent drag reduction. *J. Fluid Mech.* **667**, 135–157.

QUADRIO, M., RICCO, P. & VIOTTI, C. 2009 Streamwise-travelling waves of spanwise wall velocity for turbulent drag reduction. *J. Fluid Mech.* **627**, 161–178.

RICCO, P. 2004 Modification of near-wall turbulence due to spanwise wall oscillations. *J. Turbul.* **5**, 024.

RICCO, P., OTTONELLI, C., HASEGAWA, Y. & QUADRIO, M. 2012 Changes in turbulent dissipation in a channel flow with oscillating walls. *J. Fluid Mech.* **700**, 77–104.

ROGERS, M. H. & LANCE, G. N. 1960 The rotationally symmetric flow of a viscous fluid in the presence of an infinite rotating disk. *J. Fluid Mech.* **7** (4), 617–631.

SHARMA, A. S., MORRISON, J. F., MCKEON, B. J., LIMEBEER, D. J. N., KOBERG, W. H. & SHERWIN, S. J. 2011 Relaminarisation of $Re = 100$ channel flow with globally stabilising linear feedback control. *Phys. Fluids* **23**, 125105.

SKOTE, M. 2012 Temporal and spatial transients in turbulent boundary layer flow over an oscillating wall. *Intl J. Heat Fluid Flow* **38**, 1–12.

TOUBER, E. & LESCHZINER, M. A. 2012 Near-wall streak modification by spanwise oscillatory wall motion and drag-reduction mechanisms. *J. Fluid Mech.* **693**, 150–200.

VIOTTI, C., QUADRIO, M. & LUCHINI, P. 2009 Streamwise oscillation of spanwise velocity at the wall of a channel for turbulent drag reduction. *Phys. Fluids* **21**, 115109.

VISWANATH, P. R. 2002 Aircraft viscous drag reduction using riblets. *Prog. Aerosp. Sci.* **38**, 571–600.

WANG, C. Y. 1989 Shear flow over a rotating plate. *Appl. Sci. Res.* **46**, 89–96.

WILLIS, A. P., HWANG, Y. & COSSU, C. 2010 Optimally amplified large-scale streaks and drag reduction in turbulent pipe flow. *E* **82**, 036321.

YOSHINO, T., SUZUKI, Y. & KASAGI, N. 2008 Drag reduction of turbulence air channel flow with distributed micro-sensors and actuators. *J. Fluid Sci. Technol.* **3**, 137–148.